Supporting Information

A Salt-Concentrated electrolyte for Aqueous Ammonium-ion Hybrid Batteries

Jianming Meng[a], Yu Song[a,b]*, Jing Wang[d]*, Peng Hei[a], Chang Liu[a], Mengxue Li[a], Yulai Lin[a], Xiao-Xia Liu[a,b,c]*

[a]Department of Chemistry, Northeastern University, 3-11, Wenhua Road, Heping district, Shenyang, 110819, China.
[b]National Frontiers Science Center for Industrial Intelligence and Systems Optimization, Northeastern University,
3-11, Wenhua Road, Heping district, Shenyang, 110819, China.
[c]Key Laboratory of Data Analytics and Optimization for Smart Industry (Northeastern University), Ministry of Education, 3-11, Wenhua Road, Heping district, Shenyang, 110819, China.
[d]State Key Laboratory of Metastable Materials Science and Technology, Yanshan University, Qinhuangdao, 066004, China.

Corresponding Author

Yu Song*, Jing Wang*, Xiao-Xia Liu*

E-mail: songyu@mail.neu.edu.cn, jwang6027@ysu.edu.cn, xxliu@mail.neu.edu.cn.

1.Experimental section

Materials: Ammonium acetate (CH_3COONH_4, 98%), anhydrous zinc acetate [$Zn(CH_3COO)_2$, 98%], cobalt nitrate hexahydrate [$Co(NO_3)_2{\cdot}6H_2O$, 98.5%], nickel nitrate hexahydrate [$Ni(NO_3)_2{\cdot}6H_2O$, 98%], potassium hydroxide (KOH, 85%), potassium nitrate (KNO_3, 99%) were received from Sinopharm Chemical Reagent Co., Ltd. Graphite foil was purchased from SGL Carbon Gmbh, Germany. All the reagents were used as received.

Electrochemical exfoliation of graphite foil (EG): The exfoliation of graphite foil was conducted in a three-electrode cell, where a piece of graphite foil (working area: 0.8 × 0.8 cm^2) was employed as the working electrode, a saturated calomel electrode (SCE) and a graphite foil (working area: 2 × 2 cm^2) as the reference and counter electrodes, respectively. Initially, the graphite foil was exfoliated in 0.5 M KOH solution using cyclic voltammetry (CV) at a scan rate of 20 mV s^{-1}, ranging from 0.5 V to 1.7 V vs. SCE for 5 cycles. Subsequently, a secondary exfoliation of graphite foil was carried out in 1 M KNO_3 solution via a constant potential technology at a potential of 1.83 V vs. SCE for 25 min. In the last step, the electrode's conductivity was recovered in 1 M KNO_3 solution by CV scan from -1.2 to 1.2 V vs. SCE at scan rate of 20 mV s^{-1} for 20 cycles. The resulting electrode was denoted as EG.

Preparation of A-CoNi DH: The Co-Ni double hydroxide electrode (CoNi DH) was electrodeposited using EG as the working electrode, SCE as the reference electrode and a piece of graphite foil as the counter electrode in a three-electrode configuration. The working electrode was CV scanned between -1 to -0.6 V vs. SCE at a scan rate of 30 mV s^{-1} for 5 cycles in an electrolyte containing 0.3 M $Co(NO_3)_2$ and 0.15 M $Ni(NO_3)_2$. The obtained electrode was denoted as CoNi DH. Then, the CoNi DH electrode was electrochemically activated in 1 M KOH electrolyte using CV scan between 0 to 0.7 V vs. SCE at a scan rate of 50 mV s^{-1} for 5 cycles. The active mass loading of A-CoNi DH was about 3.1 mg cm^{-2}.

Characterization: X-ray diffraction (XRD, X'Pert Pro, PANalytical B.V., Netherlands) analysis were performed to study the crystalline phase of the materials. The morphology of the samples was analyzed by scanning electron microscopy (SEM, HITACHI, SU8010, Japan). Fourier transform infrared spectroscopy was conducted by a Fourier transform infrared spectrometer (VERTEX70, Bruker, Germany). The valence of the elements was determined via the XPS spectrometer (ESCALAB 250 Xi, Thermo Scientific Escalab, USA). The ion conductivity of the solution was obtained via a conductivity meter (FE38, Mettler Toledo). The active mass loading of electrode was tested using Sartorius BT 25 S semi-micro balance.

Electrochemical characterization: The electrochemical properties of the A-CoNi DH electrode were tested in a three-electrode cell containing differently concentrated CH_3COONH_4 aqueous solutions [1, 5, 15 and 20 mol kg^{-1} (m)], with a graphite foil and SCE as the counter and reference electrodes, respectively. The ammonium-ion hybrid battery [Zn | 15 m CH_3COONH_4 + 2 m $Zn(CH_3COO)_2$ | A-CoNi DH] and Zn-ion battery [Zn | 2 m $Zn(CH_3COO)_2$ | A-CoNi DH] were assembled using A-CoNi DH cathode, zinc foil (thickness: 150 µm, diameter: 1.2 cm) anode and glass microfiber filter separator with 15 m CH_3COONH_4 + 2 m $Zn(CH_3COO)_2$ and 2 m $Zn(CH_3COO)_2$ aqueous solution (100 µL) as the electrolytes, respectively.

The electrochemical preparation of the A-CoNi DH electrode was carried out using VMP3 Bio-Logic-Science multichannel electrochemical analyzer. Subsequently, the electrochemical performances of the A-CoNi DH electrode and the devices were evaluated using VMP3 and CT3001A LAND battery testing system, respectively. CHI 660D electrochemical workstation was used to test the electrochemical impedance spectroscopy (EIS) of the electrodes. The EIS spectra of the materials were recorded over a frequency range from 5×10^5 to 0.01 Hz.

2. Computational details

The dynamic calculations were performed using the CP2K package. The simulations were sampled by the canonical (NVT) ensemble employing Nose-Hoover thermostats with a time step of 2.0 fs at a fifinite temperature of 300 K[1, 2] for more than 20 ps. The GTH pseudopotentials[3, 4] were chosen to describe the core electrons. The wave functions were expanded in optimized double-ζ Gaussian basis sets[5] and the plane waves were expanded with a cutoff energy of 350 Rydberg. Dispersion correction was applied in all calculations with the DFT-D3 method. [6, 7]

The DFT[8, 9] calculations are conducted using VASP,[10, 11] based on projector augmented wave(PAW) method.[12] The PBE exchange-correlation functional within the generalized gradient approximation(GGA) is employed.[13] The cutoff energy of the kinetic energy is 500eV. The k-mash in the Brillouin zone is 1×1×1 via Monkhorst-Pack method.[14] The energy convergence tolerance is 1.0×10^{-5} eV, and the force certification is 0.05 eV/Å. The van der Waals(vdW) interaction is involved via the semi-empirical DFT-D2 field method.[6, 15]

3. Supplementary figures

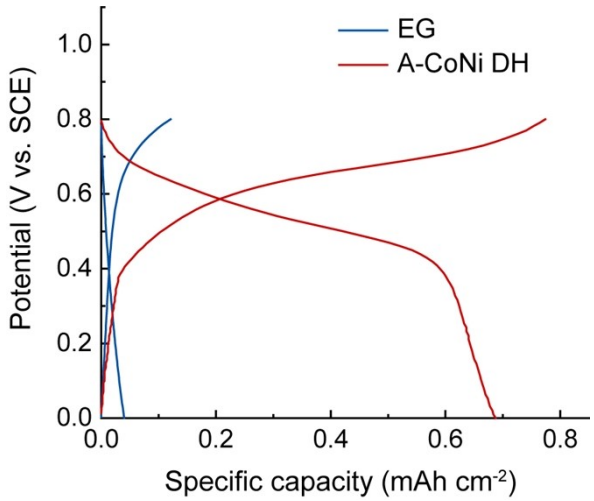

Fig. S1 Galvanostatic charge/discharge curves of the EG substrate and A-CoNi DH at the current density of 2.7 mA cm^{-2} (0.85 A g^{-1}).

As shown in Fig. S1, the EG substrate exhibited low capacities of 0.04 mAh cm^{-2} at the current density of 2.7 mA cm^{-2}. The substrate only delivers around 5.8 % of the overall capacity of the A-CoNi DH electrode. The actual contribution should be much lower considering that the surface of EG is covered by active materials. Therefore, the active material on the electrode contributes to the majority of the electrochemical activity of the electrode.

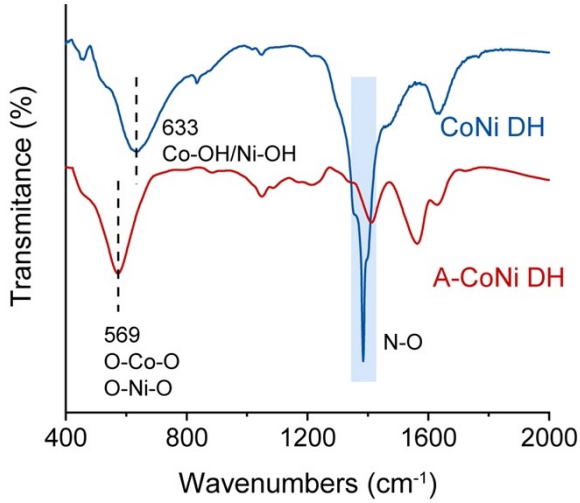

Fig. S2 FTIR spectra of CoNi DH and A-CoNi DH.

After activation, the weak signal of Co-OH and Ni-OH at around 633 cm^{-1} for CoNi DH are disappeared and O-Co-O/O-Ni-O vibrations appeared at 569 cm^{-1} , which could be due to the introduced H vacancies during the electrochemical activation, in accord with the previous reported papers.[16, 17]

During the electrode material fabrication, we used 0.3 M $Co(NO_3)_2{\cdot}6H_2O$ and 0.15 M $Ni(NO_3)_2{\cdot}6H_2O$ plating electrolyte. Therefore, NO_3^- ions would be trapped in the deposited CoNi double hydroxide material. As shown in Fig. S2, we can see the obvious NO_3^- signal at 1384 cm^{-1} in the FTIR spectrum of the as deposited material. Upon the electrochemical activation process, though large amount of NO_3^- ions were extracted during the cyclic voltammetry treatment in KOH electrolyte, a small amount NO_3^- ions remain in the material.

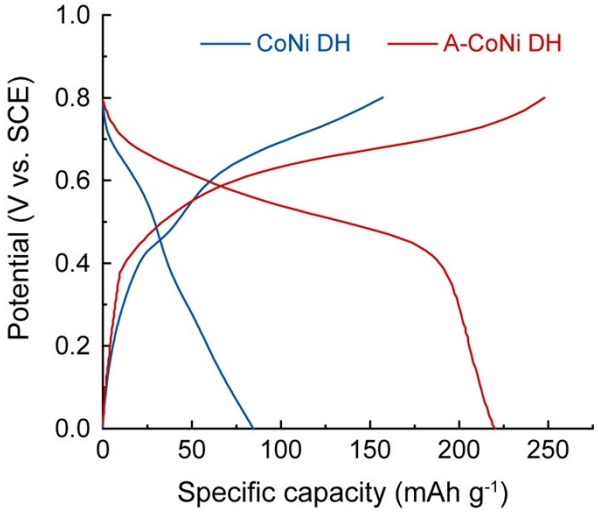

Fig. S3 Galvanostatic charge/discharge curves of CoNi DH and A-CoNi DH in 15 m CH_3COONH_4 electrolyte.

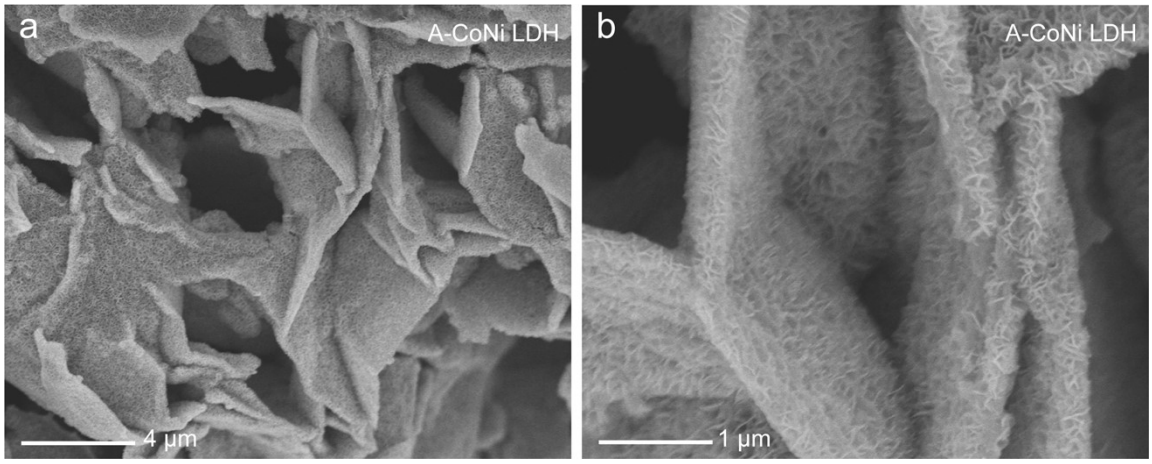

Fig. S4 SEM images of A-CoNi DH.

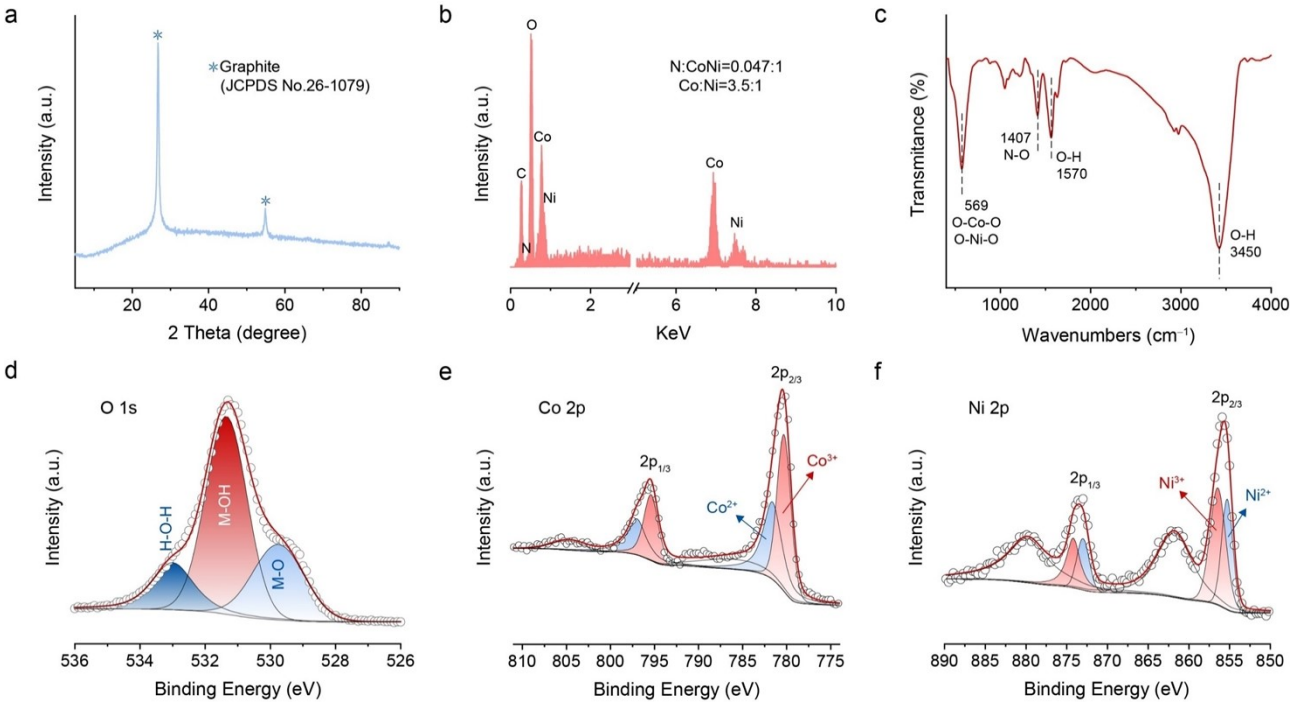

Fig. S5 (a) XRD patterns, (b) EDS, (c) FTIR, (d) XPS O 1s, (e) XPS Co 2p, and (f) XPS Ni 2p spectra of the A-CoNi DH electrode.

The EDS results indicate that the atomic ratio of N:(Co+Ni) is about 0.047:1, and the ratio of Co: Ni is about 3.5 :1. The content of N should come from the intercalated NO_3^- during the electro-deposition (Fig. S5b). As shown in Fig. S5c, the peaks at 569 cm^{-1}, 1570 cm^{-1}, and 3450 cm^{-1} are ascribed to O-Co-O/O-Ni-O vibrations, the bending and stretching vibrations of -OH groups, respectively.[18-20] The weak signal of Co-OH and Ni-OH at around 646 cm^{-1} could be due to the introduced H vacancies during the electrochemical activation, in accord with the previous reported papers.[17, 21] XPS O 1s spectra can be fitted into Metal-O (529.8 eV), Metal-OH (531.4 eV) and H-O-H (533 eV) components, and the content ratio of metal-O/metal-OH is about 0.47:1. The emerging metal-O species also indicated the presence of H vacancies in the activated hydroxide materials.[17, 20, 22] XPS Co 2p and XPS Ni 2p spectra suggest the average valence states of Co and Ni in A-CoNi DH are 2.54 and 2.42, respectively. According to the above results, the possible molecular formula of A-CoNi DH is about $Co_{0.78}Ni_{0.22}O_{0.6}(OH)_{1.27}(NO_3)_{0.05}$. Assuming that both Co and Ni atoms in the material can transfer one electron during the charge/discharge process, the calculated theoretical capacity of the material is about 287 mAh g^{-1}.

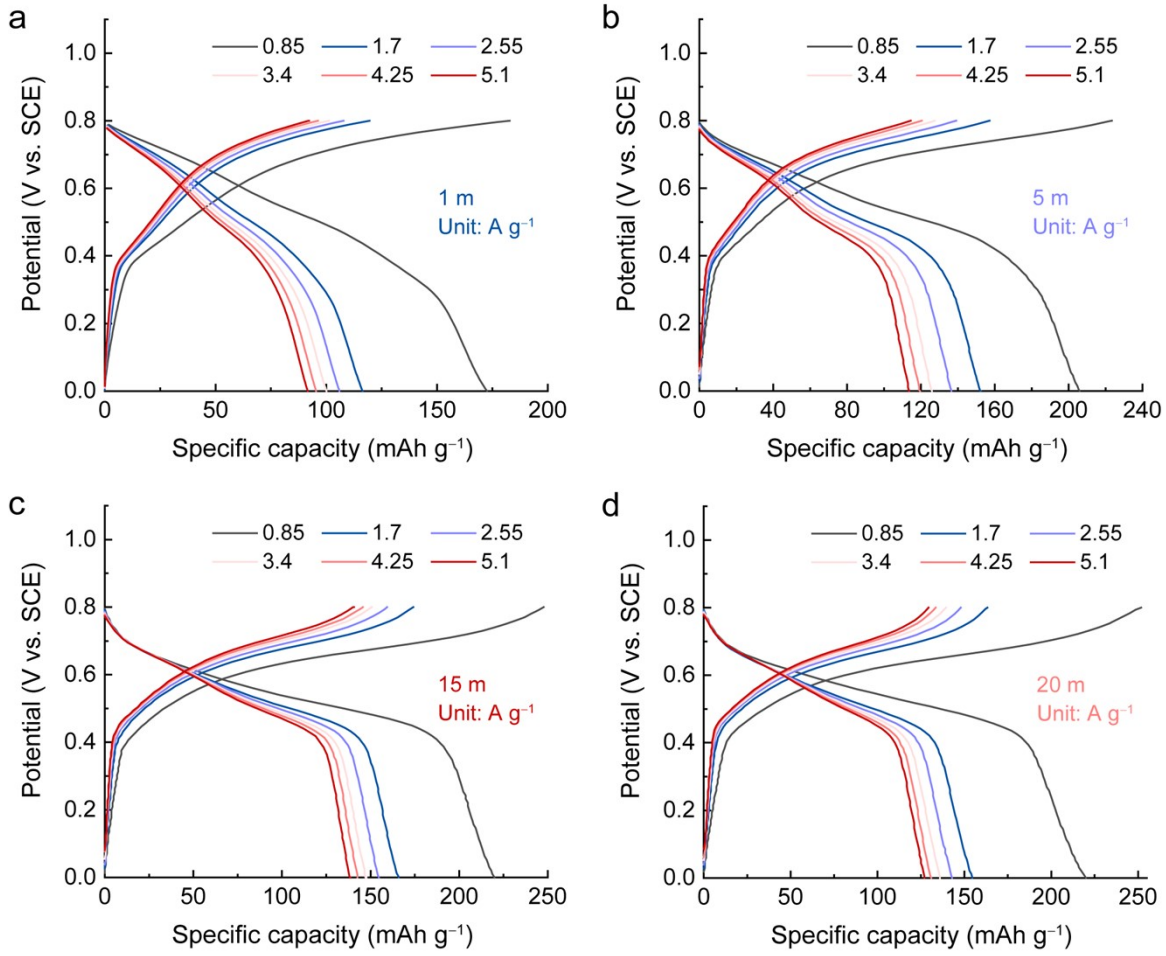

Fig. S6 Galvanostatic charge/discharge curves of the A-CoNi DH electrode in different concentrations of ammonium acetate electrolyte. (a) 1m, (b) 5 m, (c)15 m, (d) 20 m.

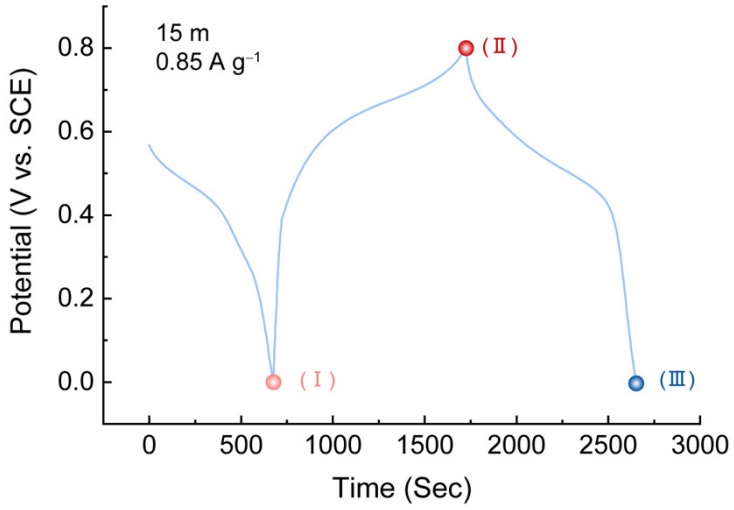

Fig. S7 Three different state of charge/discharge of the A-CoNi DH electrode used for mechanical study.

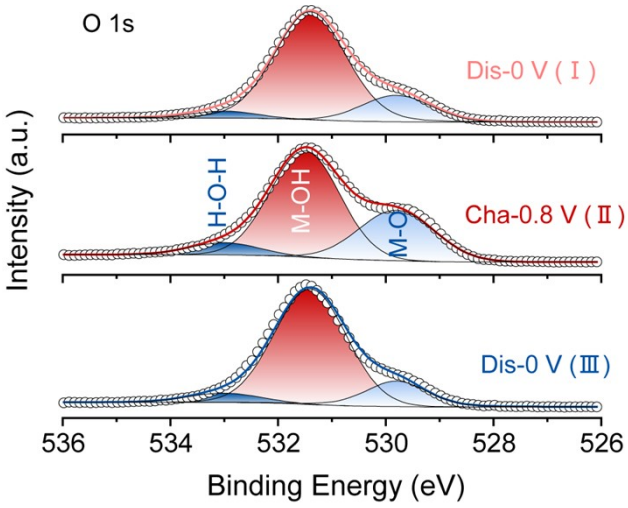

Fig. S8 XPS O 1s spectra of the A-CoNi DH electrode at different states of charge/discharge.

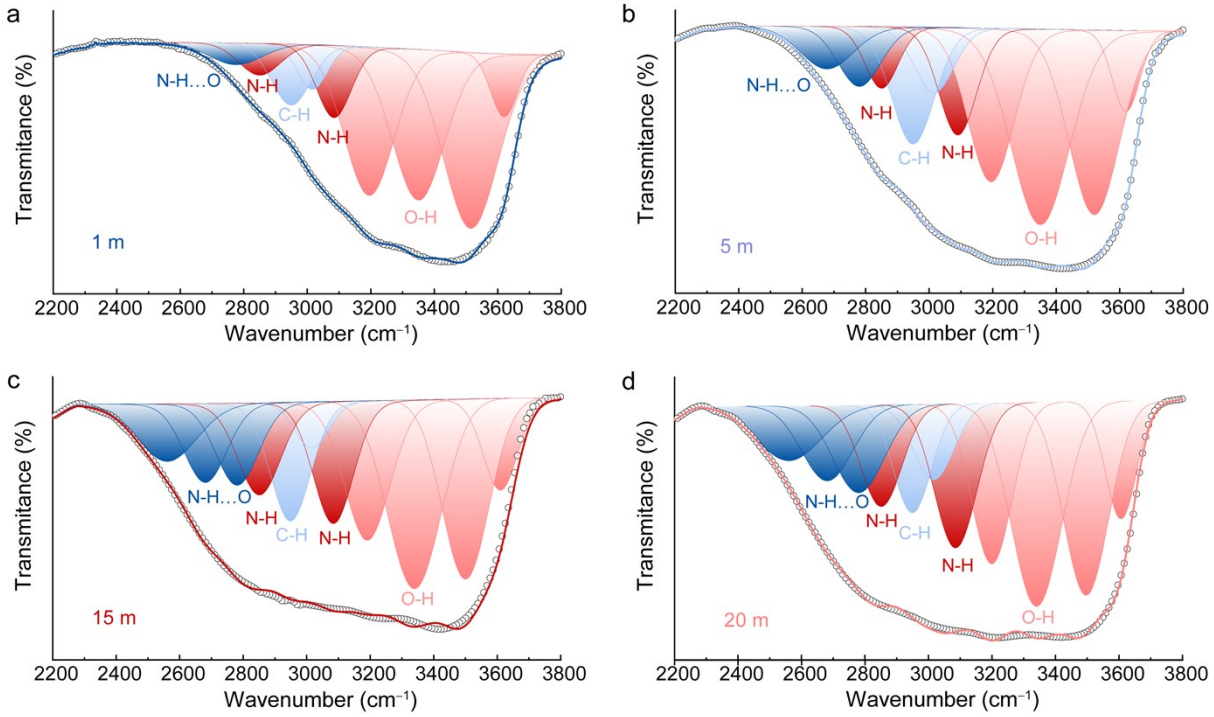

Fig. S9 FTIR spectrum of different concentrations of ammonium acetate electrolytes. (a) 1m, (b) 5 m, (c)15 m, (d) 20 m.

For O-H components, the higher wavenumber peak at 3620 cm^{-1} can be attributed to the non-hydrogen bond. Two intermediate vibrations at 3515 cm^{-1} and 3350 cm^{-1} are assigned to the weak hydrogen bond, and the lowest wavenumber at 3195 cm^{-1} labeled as strong hydrogen bond. In addition, 3084 cm^{-1} and 2850 cm^{-1} are attributed to N-H peaks, 3016 cm^{-1} and 2949 cm^{-1} are attributed to C-H peaks, 2780 cm^{-1}, 2681 cm^{-1} and 2561 cm^{-1} are ascribed to N-H…O peaks, respectively.[23, 24]

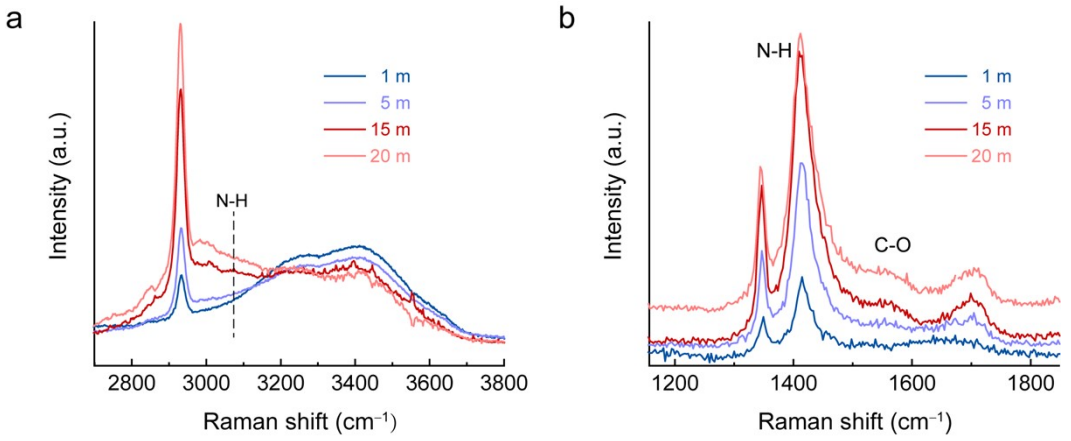

Fig. S10 Raman spectrum of different concentrations of ammonium acetate electrolyte.

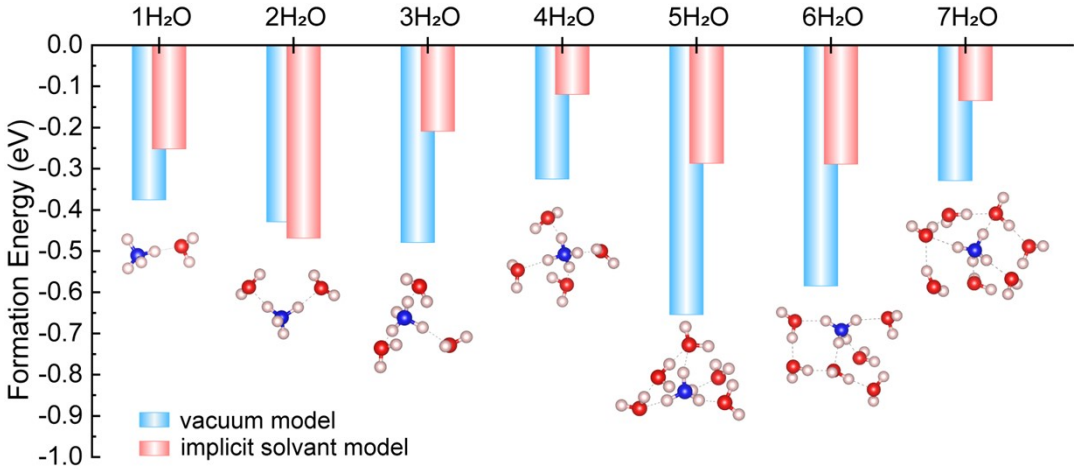

Fig. S11 The number of water molecules in the solvated shell and formation energy of ammonium.

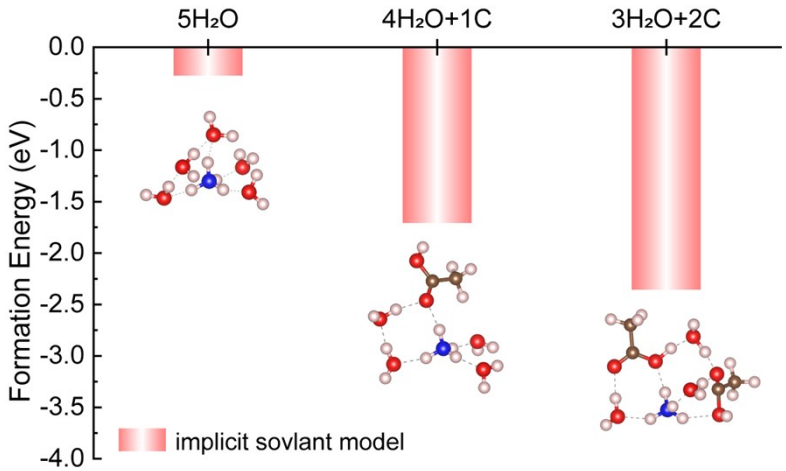

Fig. S12 Solvation structure and formation energy of ammonium in 15 m CH_3COONH_4.

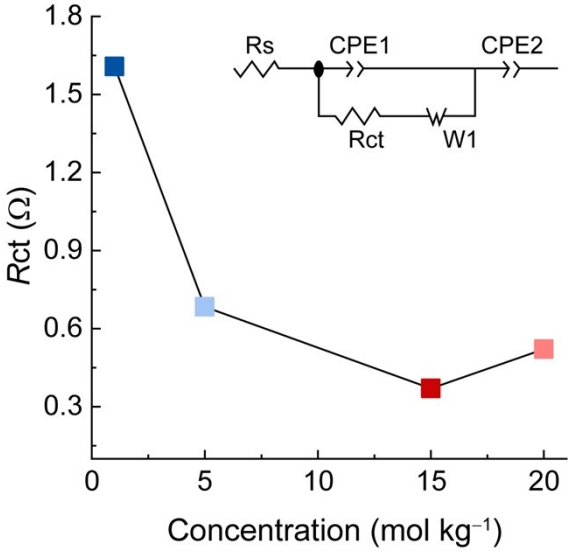

Fig. S13 The corresponding Rct values obtained from Fig. 3a, inset shows the equivalent circuit.

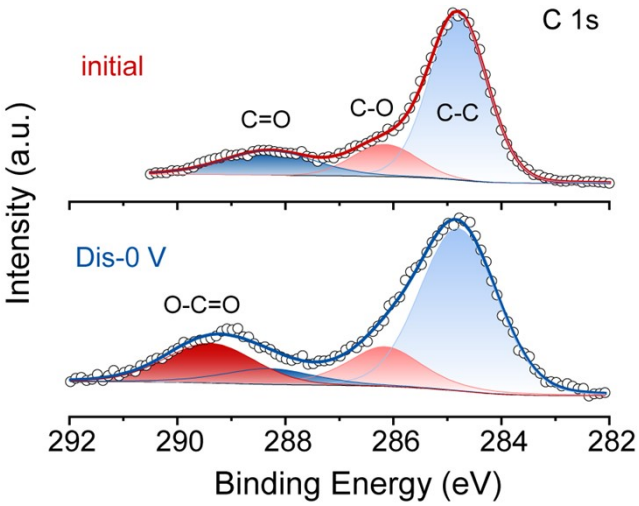

Fig. S14 XPS C 1s spectra of the A-CoNi DH electrode at different states.

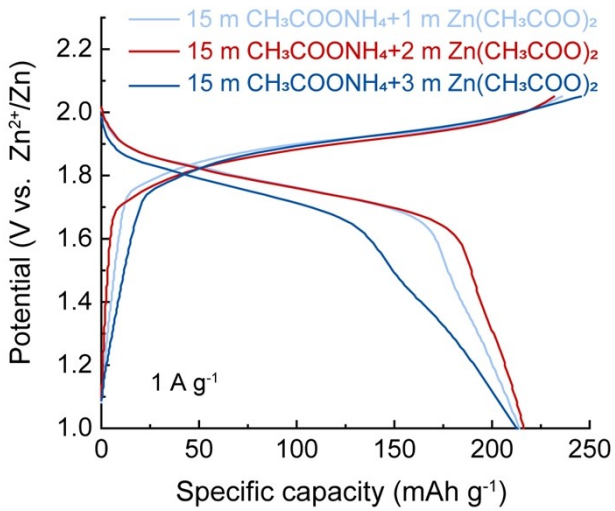

Fig. S15 Charge/discharge curves of A-CoNi DH electrode in 15 m CH_3COONH_4 + 1 m Zn(CH3COO)$_2$, 15 m CH_3COONH_4 + 2 m $Zn(CH_3COO)_2$ and 15 m CH_3COONH_4+ 3 m $Zn(CH_3COO)_2$ electrolytes.

We have optimized the Zn^{2+} concentration in this study. We collected the charge/discharge profiles of the A-CoNi DH electrode in 15 m CH_3COONH_4 + 1 m $Zn(CH_3COO)_2$, 15 m CH_3COONH_4 + 2 m $Zn(CH_3COO)_2$ and 15 m CH_3COONH_4 + 3 m $Zn(CH_3COO)_2$ electrolytes, respectively. As shown in Fig. S15, the electrode in 1 m and 2 m $Zn(CH_3COO)_2$ electrolytes exhibited similar capacities. Yet, further increasing the $Zn(CH_3COO)_2$ concentration to 3 m led to the decreased capacity and the discharge plateau, which could be due to the high viscosity of the electrolyte. Therefore, we chose the 15m CH_3COONH_4 + 2 m $Zn(CH_3COO)_2$ electrolyte to assemble the hybrid device.

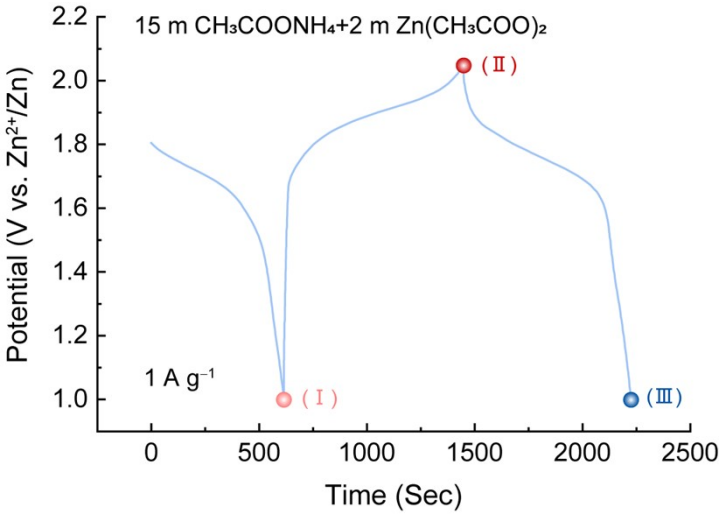

Fig. S16 Three different states of charge/discharge of the A-CoNi DH electrode used for mechanism study.

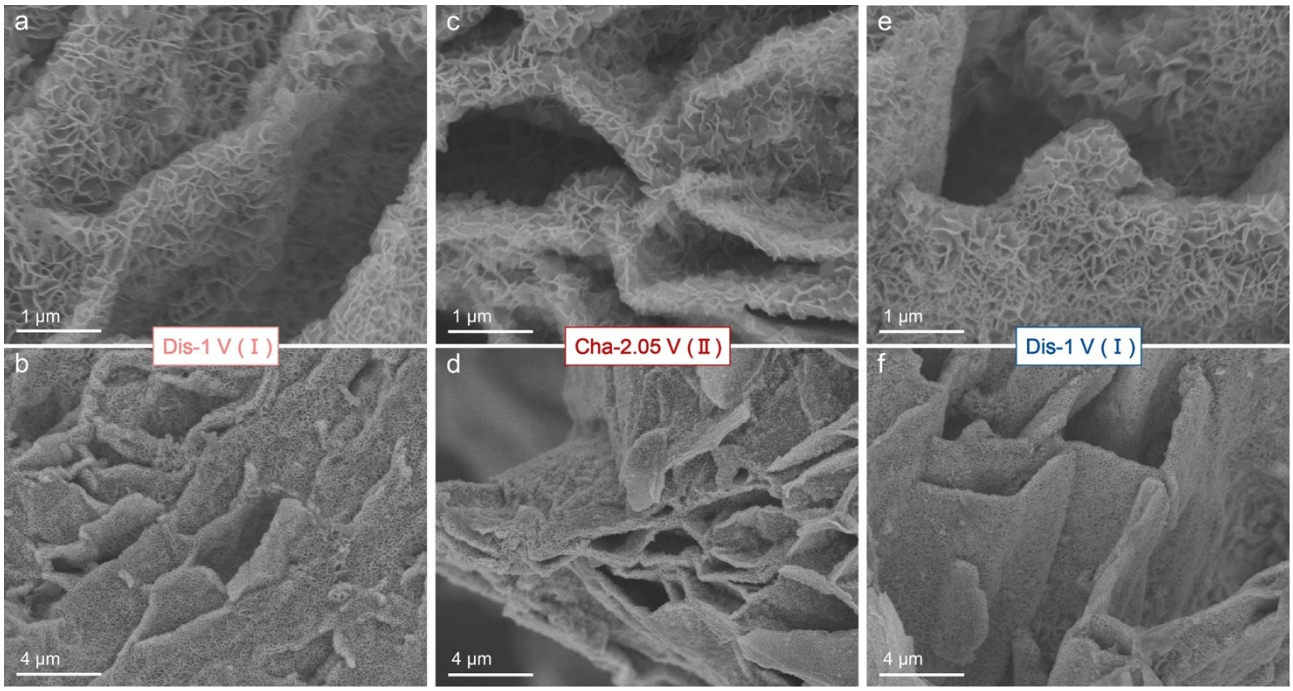

Fig. S17 SEM images of the A-CoNi DH electrode at different states of charge. (a) and (b) 1 V, (c) and (d) 2.05 V, (e) and (f) 1 V.

These images suggest that the nanosheet structure of A-CoNi DH did not change during the charge storage process. No basic zinc salt by-products were observed.

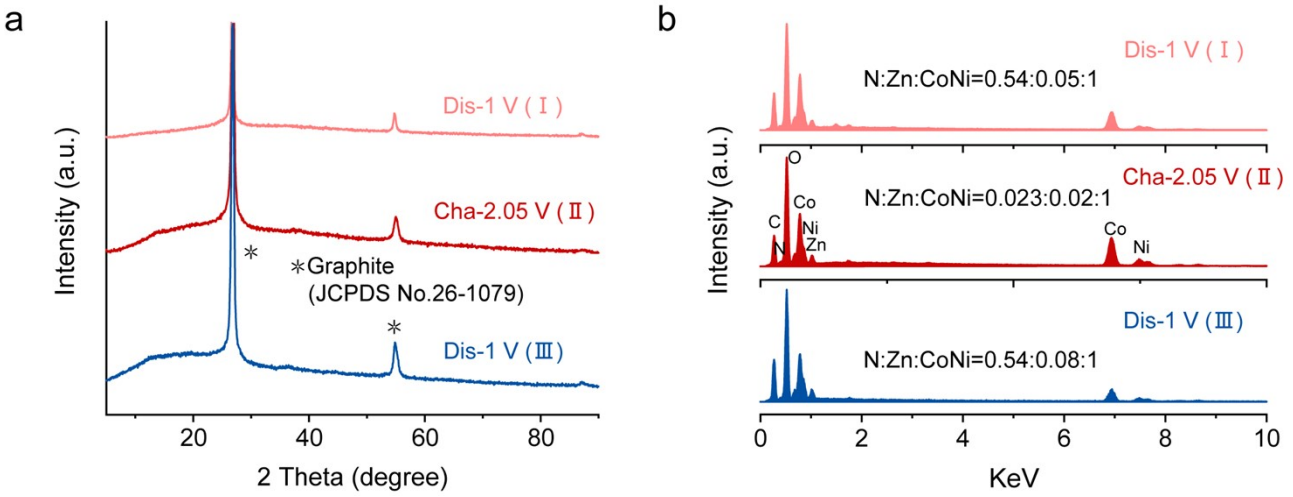

Fig. S18 (a) XRD patterns, (b) EDS spectra of A-CoNi DH electrode at different states of charge/discharge.

For the ex-situ XRD spectra, in addition to the peaks for graphite substrate (JCPDS No.26-1079), we did not observe other peaks, further confirming no by-products was generated. Upon discharging from 2.05 to 1 V *vs.* Zn^{2+}/Zn, the content of N slightly increased and the Zn content remained stable, suggesting that NH_4^+ participated in the charge storage of A-CoNi DH, rather than Zn^{2+}.

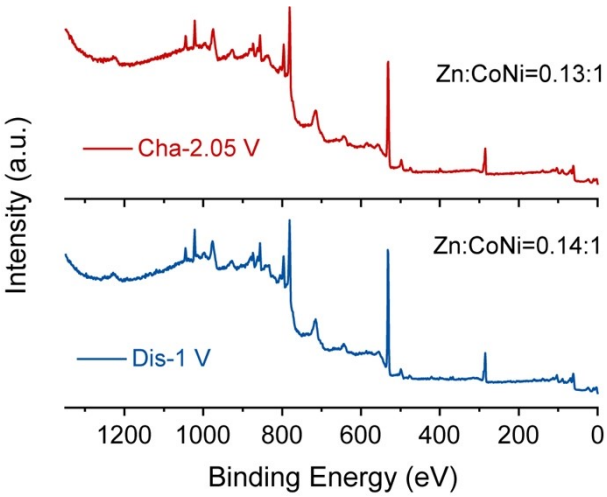

Fig. S19 XPS survey spectra of the A-CoNi DH electrode at different discharge states.

We further collected the XPS spectra of the electrode at the charged and discharged states in 15 m CH_3COONH_4 + 2 m $Zn(CH_3COO)_2$ electrolytes, respectively. After discharging, the content of Zn in the electrodes is basically unchanged, in accord with the EDS results. The Zn signal on the electrode surface could be from the adsorbed $Zn(CH_3COO)_2$.

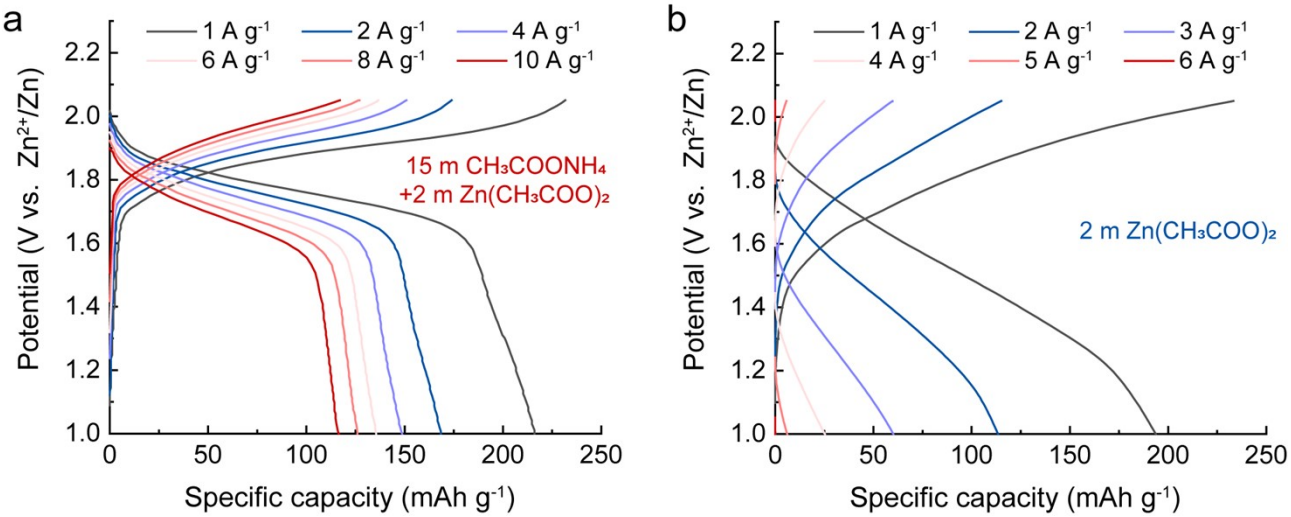

Fig. S20 Galvanostatic charge/discharge curves of the A-CoNi DH electrode in different electrolytes. (a) 15 m CH_3COONH_4 + 2 m $Zn(CH_3COO)_2$, (b) 2 m $Zn(CH_3COO)_2$.

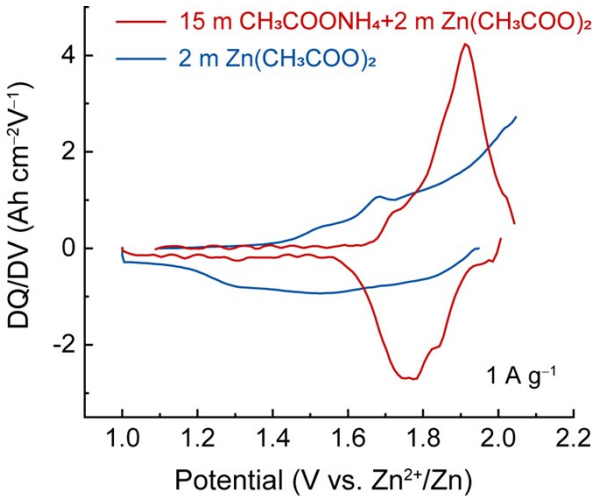

Fig. S21 Comparison of differential capacity curves the A-CoNi DH in 2 m $Zn(CH_3COO)_2$ and 15 m CH_3COONH_4 + 2 m $Zn(CH_3COO)_2$ electrolyte.

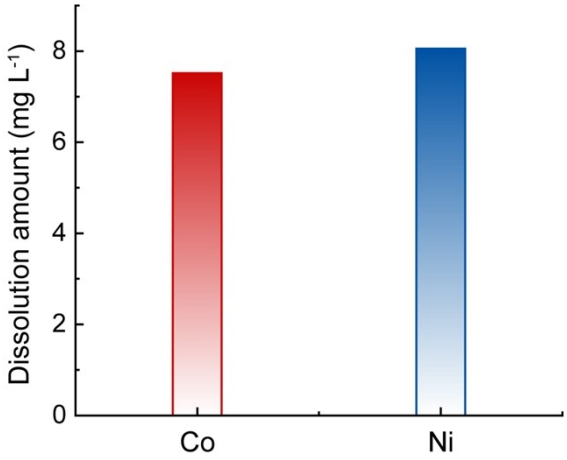

Fig. S22 ICP results of the electrolyte after 200 charge/discharge cycles.

4. Supplementary tables

Table S1. The Zn^{2+} ion diffusion barrier in the electrolyte obtained using AIMD simulation.

T/K	1000/T	Slope	*D*	log*D*
300K	3.33	1.36325	0.2272	-4.644
450K	2.22	1.18415	0.1974	-4.704
600K	1.67	3.40528	0.5675	-4.246
900K	1.11	12.21121	2.0352	-3.691
1200K	0.83	5.62597	0.9377	-4.028

Table S2. The NH_4^+ ion diffusion barrier in the electrolyte obtained using AIMD simulation.

T/K	1000/T	Slope	*D*	log*D*
300K	3.33	2.65231	0.4421	-4.354
450K	2.22	5.41932	0.9032	-4.044
600K	1.67	7.15723	1.1929	-3.923
900K	1.11	20.7102	3.4517	-3.462
1200K	0.83	21.7011	3.6169	-3.442

We calculated the ion diffusion barrier in the electrolyte using the AIMD simulation results. That is, we first derived the diffusion coefficient (*D*) using Einstein eqution ($D = \lim_{t\to\infty}\left[\frac{1}{2dt}\left\langle\left[\vec{r}(t)\right]^2\right\rangle\right]$), and the mean square displacement (MSD) from the AIMD. Then five different *D* were calculated from different temperatures, *i.e.*, 300K, 450K, 600K, 900K and 1200K. The slope of log(*D*) *vs* 1000/*T* is the diffusion barrier according to Arrhenius equation ($D = D_0 \exp\left(-\frac{E_a}{k_B T}\right)$). Results indicate that the cations in the hybrid electrolyte exhibit similar diffusion barriers, *i.e.*, 76 meV for NH_4^+ and 70 meV for Zn^{2+} (Table S1 and S2). Combining with the EDS and XPS data shown in Fig. R4, we believe that the dominant charge carrier in the cathode is NH_4^+, which could be due to the facilitated NH_4^+ adsorption on the electrode surface as well as the ultra-high concentration of NH_4^+ in the hybrid electrolyte.

Table S3. Performance summary of conventional cathode materials for AIBs.

Sample	Specific Capacity (*maximum*)	Average discharge voltage (*V*)
Ni-Co LDH//VO_x@PPy[25]	104.5	0.71
MnAl-LDH//PTCDI[26]	57.7	0.7
CuFe PBA//MoO_3[27]	41.6	0.5
$(NH_4)_{0.5}V_2O_5$//h-WO_3[28]	40	0.85
$(NH_4)_{1.47}Ni[Fe(CN)_6]_{0.88}$//PTCDI[29]	41	1
PI/NDC/CNT//PANI/CNF[30]	136.7	0.84
MnO_2//Zn[31]	301.2	1.3
Co–Mn PBAs//Zn[32]	99.7	1.4
ZnHCF//Zn[33]	65.4	1.7
VS_2/VO_x//Zn[34]	301	0.9
$VOPO_4 \cdot xH_2O$//Zn[35]	170	1.35
$Na_3V_2(PO_4)_2F_3$//Zn[36]	64.7	1.62
CuHCF//Zn(hybrid)[37]	70.4	1.8
Na-FeHCF//Zn (hybrid)[38]	73.6	1.3
MnO_2//Zn (hybrid)[39]	365	1.35
A-CoNi DH //Zn (hybrid)	216	1.7 V

Table S4. Comparison of energy and power density of conventional cathode materials for AIBs.

Sample	Energy density ($Wh\ kg^{-1}$)	Power density ($W\ kg^{-1}$)
Ni-Co LDH//VOx@PPy[25]	74.1	75.6
MnAl-LDH//PTCDI[26]	45.8	163.5
CuFe PBA//MoO_3[27]	21.3	277
$(NH_4)_{0.5}V_2O_5$//h-WO_3[28]	34	~ 409
$(NH_4)_{1.47}Ni[Fe(CN)_6]_{0.88}$//PTCDI[29]	63	43
PI/NDC/CNT//PANI/CNF[30]	114.3	18600
γ-MnO_2//WO_3[40]	64.9	2339
CuHCF//Zn(hybrid)[37]	114	458
Na-FeHCF//Zn (hybrid)[38]	81.7	286
MnO_2//Zn (hybrid)[39]	486	675
A-CoNi DH (This work)	368	1704

Reference

1 W. G. Hoover, Canonical dynamics: equilibrium phase-space distributions, *Phys. Rev. A*, 1985, **31**, 1695.

2 G. J. Martyna, M. L. Klein and M. Tuckerman, Nosé-hoover chains: the canonical ensemble via continuous dynamics, *J. Chem. Phys.*, 1992, **97**, 2635.

3 S. Goedecker, M. Teter and J. Hutter, Separable dual-space gaussian pseudopotentials, Phys. Rev. B, 1996, **54**, 1703.

4 C. Hartwigsen, S. Goedecker and J. Hutter, Relativistic separable dual-space gaussian pseudopotentials from H to Rn, *Phys. Rev. B*, 1998, **58**, 3641.

5 J. VandeVondele and J. Hutter, Gaussian basis sets for accurate calculations on molecular systems in gas and condensed phases, *J. Chem. Phys.*, 2007, **127**, 114105.

6 S. Grimme, J. Antony, S. Ehrlich and H. Krieg, A consistent and accurate ab initio parametrization of density functional dispersion correction (DFT-D) for the 94 elements H-Pu, *J. Chem. Phys.*, 2010, **132**, 154104.

7 S. Grimme, S. Ehrlich and L. Goerigk, Effect of the damping function in dispersion corrected density functional theory, *J. Comput. Chem.*, 2011, **32**, 1456-1465.

8 W. Kohn and L. J. Sham, Self-consistent equations including exchange and correlation effects, *Phys. Rev.*, 1965, **140**, 1133.

9 P. Hohenberg and W. Kohn, Inhomogeneous electron gas, *Phys. Rev.*, 1964, **136**, 864.

10 G. Kresse and J. Furthmuller, Efficiency of ab-initio total energy calculations for metals and semiconductors using a plane-wave basis set, Comput. *Mater. Sci.*, 1996, **6**, 15.

11 G. Kresse and J. Furthmuller, Efficient iterative schemes for ab initio total-energy calculations using a plane-wave basis set, *Phys. Rev. B*, 1996, **54**, 11169.

12 J. P. Perdew, K. Burke and M. Ernzerhof, Generalized gradient approximation made simple, *Phys. Rev. Lett.*, 1996, **77**, 3865.

13 P. E. Blöchl, Projector augmented-wave method, *Phys. Rev. B*, 1994, **50**, 17953.

14 H. J. Monkhorst and J. D. Pack, Special points for Brillouin-zone integrations, *Phys. Rev. B*, 1976, **13**, 5188.

15 S. Grimme, Semiempirical GGA-type density functional constructed with a long-range dispersion correction, *J. Comput. Chem.* 2006, **27**, 1787.

16 C. Liu, M. Li, J. Meng, P. Hei, J. Wang, Y. Song and X. X. Liu, Electrochemical storage of ammonium versus metal ions in bimetallic hydroxide for sustainable aqueous batteries, *Adv. Funct. Mater.*, 2023, DOI: 10.1002/adfm.202310437.

17 J. Meng, Y. Song, Z. Qin, Z. Wang, X. Mu, J. Wang and X. X. Liu, Cobalt-nickel double hydroxide toward mild aqueous zinc-ion batteries, *Adv. Funct. Mater.*, 2022, **32**, 2204026.

18 H. Chu, Y. Zhu, T. Fang, J. Hua, S. Qiu, H. Liu, L. Qin, Q. Wei, Y. Zou, C. Xiang, F. Xu and L. Sun, Solvothermal synthesis of cobalt nickel layered double hydroxides with a three-dimensional nano-petal structure for high-performance supercapacitors, *Sustain. Energy Fuels*, 2020, **4**, 337-346.

19 Z. Li, H. Duan, M. Shao, J. Li, D. O'Hare, M. Wei and Z. L. Wang, Ordered-vacancy-induced cation intercalation into layered double hydroxides: A general approach for high-performance supercapacitors, *Chem*, 2018, **4**, 2168-2179.

20 Y Song, Q. Pan, H. Lv, D. Yang, Z. Qin, M. Y. Zhang, X. Sun and X. X. Liu, Ammonium-ion storage using electrodeposited manganese oxides, *Angew. Chem. Int. Ed.*, 2021, **60**, 5718-5722.

21 M. Wei, Q. Huang, Y. Zhou, Z. Peng and W. Chu, Ultrathin nanosheets of cobalt-nickel hydroxides hetero-structure via electrodeposition and precursor adjustment with excellent performance for supercapacitor, *J. Energy Chem.*, 2018, **27**, 591-599.

22 Y. Zhang, B. Ouyang, J. Xu, G. Jia, S. Chen, R. S. Rawat and H. J. Fan, Rapid synthesis of cobalt nitride nanowires: Highly efficient and low-cost catalysts for oxygen evolution, *Angew. Chem. Int. Ed.*, 2016, **128**, 8812-8816.

23 G. Ramis and G. Busca, FTIR spectra of adsorbed n-butylamine, *J. Mol. Struct.*, 1989, **193**, 93-100.

24 G. Dovbeshko, N. Gridina, E. Kruglova and O. Pashchuk, FTIR spectroscopy studies of nucleic acid damage, *Talanta*, 2000, **53**, 233-246.

25 X. Mu, Y. Song, Z. Qin, J. Meng, Z. Wang and X. X. Liu, Core-shell structural vanadium oxide/polypyrrole anode for aqueous ammonium-ion batteries, *Chem. Eng. J.*, 2023, **453**,139575.

26 Q. Liu, F. Ye, K. Guan, Y. Yang, H. Dong, Y. Wu, Z. Tang and L. Hu, MnAl layered double hydroxides: A robust host for aqueous ammonium-ion storage with stable plateau and high capacity, *Adv. Energy Mater.*, 2022, **13**, 2202908.

27 G. Liang, Y. Wang, Z. Huang, F. Mo, X. Li, Q. Yang, D. Wang, H. Li, S. Chen and C. Zhi, Initiating hexagonal MoO_3 for superb-stable and fast NH_4^+ storage based on hydrogen bond chemistry, *Adv. Mater.*, 2020, **32**, 1907802.

28 Y. Z. Zhang, J. Liang, Z. Huang, Q. Wang, G. Zhu, S. Dong, H. Liang and X. Dong, Ionically conductive tunnels in h-WO_3 enable high-rate NH_4^+ storage, *Adv. Sci.*, 2022, **9**, 2105158.

29 X. Wu, Y. Qi, J. J. Hong, Z. Li, A. S. Hernandez and X. Ji, Rocking-chair ammonium-ion battery: A highly reversible aqueous energy storage system, *Angew. Chem. Int. Ed.*, 2017, **56**, 13026-13030.

30 G. Zhou, X. An, C. Zhou, Y. Wu, Y.-E. Miao and T. Liu, Highly porous electroactive polyimide-based nanofibrous composite anode for all-organic aqueous ammonium dual-ion batteries, *Compos. Commun.*, 2020, **22**, 100519.

31 B. Wu, G. Zhang, M. Yan, T. Xiong, P. He, L. He, X. Xu and L. Mai, Graphene scroll-coated α-MnO_2 nanowires as high-performance cathode materials for aqueous zn-ion battery, *Small*, 2018, **14**, 1703850.

32 Y. Zeng, X. F. Lu, S. L. Zhang, D. Luan, S. Li and X. W. Lou, Construction of Co-Mn prussian blue analog hollow spheres for efficient aqueous zn-ion batteries, *Angew. Chem. Int. Ed.*, 2021, **60**, 22189-22194.

33 L. Zhang, L. Chen, X. Zhou and Z. Liu,Towards high-voltage aqueous metal-ion batteries beyond 1.5 V: The zinc/zinc hexacyanoferrate system, *Adv. Energy Mater.*, 2015, **5**, 1400930.

34 D. Yu, Z. Wei, X. Zhang, Y. Zeng, C. Wang, G. Chen, Z. X. Shen and F. Du, Boosting Zn^{2+} and NH_4^+ storage in aqueous media via in-situ electrochemical induced VS_2/VO_x heterostructures, *Adv. Funct. Mater.*, 2020, **31**, 2008743.

35 H. Y. Shi, Y. Song, Z. Qin, C. Li, D. Guo, X. X. Liu and X. Sun, Inhibiting $VOPO_4{\cdot}xH_2O$ decomposition and dissolution in rechargeable aqueous zinc batteries to promote voltage and capacity stabilities, *Angew. Chem. Int. Ed.*, 2019, **58**, 16057-16061.

36 W. Li, K. Wang, S. Cheng and K. Jiang, A long-life aqueous zn-ion battery based on $Na_3V_2(PO_4)_2F_3$ cathode, *Energy Storage Mater.*, 2018, **15**, 14-21.

37 C. Li, J. Wu, F. Ma, Y. Chen, L. Fu, Y. Zhu, Y. Zhang, P. Wang, Y. Wu and W. Huang, High-rate and high-voltage aqueous rechargeable zinc ammonium hybrid battery from selective cation intercalation cathode, *ACS Appl. Energy Mater.*, 2019, **2**, 6984-6989.

38 C. Li, D. Zhang, F. Ma, T. Ma, J. Wang, Y. Chen, Y. Zhu, L. Fu, Y. Wu and W. Huang, A high-rate and long-life aqueous rechargeable ammonium zinc hybrid battery, *ChemSusChem*, 2019, **12**, 3732-3736.

39 S. Wang, Z. Yuan, X. Zhang, S. Bi, Z. Zhou, J. Tian, Q. Zhang and Z. Niu, Non-metal ion co-insertion chemistry in aqueous Zn/MnO_2 batteries, *Angew. Chem. Int. Ed.*, 2021, **60**, 7056-7060.

40 X. Wen, J. Lou, K. Xiang, W. Zhou, C. Zhang and H. Chen, High-performance monoclinic WO_3 nanospheres with the novel NH_4^+ diffusion behaviors for aqueous ammonium-ion batteries, *Chem. Eng. J.*, 2023, **458**, 141381.